Physica B: Condensed Matter 551 (2018) 339–346

Contents lists available at ScienceDirect

Physica B: Condensed Matter

journal homepage: www.elsevier.com/locate/physb

Weak values from strong interactions in neutron interferometry

Tobias Denkmayr [a], Justin Dressel [c,d], Hermann Geppert-Kleinrath [a], Yuji Hasegawa [a,b], Stephan Sponar [a,*]

[a] Atominstitut - TU Wien, Stadionallee 2, 1020 Vienna, Austria
[b] Division of Applied Physics, Hokkaido University Kita-ku, Sapporo 060-8628, Japan
[c] Institute for Quantum Studies, Chapman University, Orange, California 92866, USA
[d] Schmid College of Science and Technology, Chapman University, Orange, California 92866, USA

ARTICLE INFO

Keywords:
Neutron
Interferometry
Spin
Weak values

ABSTRACT

In their original framework weak values must be measured by weak measurements that are minimally disturbing, meaning that the coupling between an investigated quantum system and a measurement device has no influence on the evolution of the system. However, under certain circumstances this weakness of the interaction is not necessary. In that case weak values can still be exactly determined from the statistics of the outcomes of arbitrary-strength generalized measurements. Here, we report an experimental procedure for neutron matter-waves that extends the notion of generalized eigenvalues for the neutron's path system to allow the exact determination of weak values using both strong and weak interactions. Experimental evidence is given that strong interactions outperform weak ones both for precision and accuracy.

1. Introduction

The *weak value* of an operator $\hat{A}$ was introduced by Aharonov, Albert and Vaidman (AAV) in Ref. [1] as "a new kind of value for a quantum variable". The weak value was operationally obtained via a specific procedure, referred to as a post-selected weak measurement, where the probed quantum system is left minimally disturbed and pursues its evolution from an initial state $|\psi_i\rangle$ towards a selected final state $|\psi_f\rangle$, without projecting the system into its eigenstates in between. If this procedure is applied, the result of averaging the weak measurements of the operator $\hat{A}$ is not the usual expectation value but rather the weak value

$$\langle\hat{A}\rangle_w = \frac{\langle\psi_f|\hat{A}|\psi_i\rangle}{\langle\psi_f|\psi_i\rangle}. \quad (1)$$

Both real and imaginary parts of this generally complex expression can be obtained separately by changing how the probe is measured. The weak value of an operator $\hat{A}$ may differ significantly from an average of the eigenvalues of an associated operator since weak values may lie far outside the eigenvalue range of the operator. The weak value has evolved from a theoretical peculiarity to a powerful experimental tool [2]: it can be applied to high precision metrology by amplifying detector signals [3–8], or as a new method for the estimation of quantum states [9–14]. In addition, weak values and weak measurement have been productively applied to quantum paradoxes such as the three-box problem [15], Hardy's paradox [16–18] and the quantum Cheshire cat [19–21].

In their original proposal in Ref. [1] AVV developed the weak value formalism in a non-relativistic quantum framework for massive quantum systems applying a modified Stern-Gerlach experiment with spin-$\frac{1}{2}$ particles. However, due to the small coherence volume of massive particle beams, an experimental demonstration of a weak value's measurement in a simple massive-particle system proved to be difficult, as a result of which the first experimental determination of a weak value was realized in a purely optical setup [28]. Significant improvements in the experimental methods and techniques of neutron interferometry [29] made it possible to fully determine the weak value of a neutron's spin operator with high precision [30]. Neutron interferometry has been established as a powerful experimental tool to investigate the foundations of quantum mechanics [31–35].

2. Theoretical framework of general-strength measurements

As introduced, the AAV formula from Eq. (1) only applies to *pure* initial and final states with intermediate *weak* measurements. So naturally the following question arises: "Is the weak value expression still operationally meaningful for impure boundary conditions and finite strength

* Corresponding author.
E-mail address: sponar@ati.ac.at (S. Sponar).
https://doi.org/10.1016/j.physb.2018.04.014
Received 7 August 2017; Received in revised form 6 April 2018; Accepted 9 April 2018
Available online 13 April 2018

measurements?" To address this question rigorously, the concept of the *contextual values* of an observable were introduced in Refs. [22–25] as a generalization of its eigenvalues that take into account the details of the specific measurement procedure. There it was shown that even for non-projective measurements one may still assign meaningful values to imperfectly correlated detector outcomes—that is, averaging carefully chosen values can recover the correct expectation value as an ensemble average, but the needed values are generally not eigenvalues. This equivalence under the averaging process can be expressed more formally as an operator identity, $\widehat{A} = \sum_a a|a\rangle\langle a| = \sum_k \alpha_k \widehat{E}_k$, where a are the eigenvalues of $\widehat{A}$ with eigenstates $|a\rangle$, and α_k are contextual values for $\widehat{A}$ with respect to a particular positive operator-valued measure (POVM) $\{\widehat{E}_k\}$, satisfying $\sum_k \widehat{E}_k = \widehat{1}$. As a clarifying note, the term "context" was originally intended to mean the measurement context, i.e. the specific POVM being used to probe the observable. However, the term has caused some confusion with the unrelated concept of contextuality as it applies to hidden variable models of the quantum theory [26,27]. We thus disambiguate the two here by referring to the values α_k as *generalized eigenvalues* of the observable $\widehat{A}$.

Using this concept of generalized eigenvalues, it was rigorously shown how conditioned averages of generalized measurements converge to the weak value as a stable limit point when the measurements become sufficiently weak [22–24]. For purity-preserving measurements such that the POVM elements $\widehat{E}_k = \widehat{M}_k^\dagger \widehat{M}_k$ factor into single Kraus operators $\widehat{M}_k$, a general conditioned average of generalized measurements in between an initial mixed state $\widehat{\rho}_i$ and a final generalized measurement POVM $\widehat{F}_f$ will have the form

$$\sum_k \alpha_k P(k|f) = \frac{\mathrm{Re}[\mathrm{Tr}(\widehat{F}_f \widehat{A} \widehat{\rho})] + \sum_k \alpha_k \mathrm{Tr}(\widehat{F}_f \mathcal{L}_k[\widehat{\rho}_i])}{\mathrm{Tr}(\widehat{F}_f \widehat{\rho}) + \mathrm{Tr}(\widehat{F}_f \mathcal{L}[\widehat{\rho}_i])}, \tag{2}$$

where the perturbation away from a generalized weak value expression $\langle \widehat{A} \rangle_\mathrm{w} = \mathrm{Re}[\mathrm{Tr}(\widehat{F}_f \widehat{A} \widehat{\rho}_i)/\mathrm{Tr}(\widehat{F}_f \widehat{\rho}_i)]$ is determined by *Lindblad* decoherence $\mathcal{L}[\widehat{\rho}_i] = \sum_k \mathcal{L}_k[\widehat{\rho}_i]$ with $\mathcal{L}_k[\widehat{\rho}_i] = -\left(\widehat{M}_k[\widehat{M}_k^\dagger, \widehat{\rho}_i] - [\widehat{M}_k, \widehat{\rho}_i]\widehat{M}_k^\dagger\right)/2$. In the case of a weak measurement, $\widehat{M}_k \approx p_k \widehat{1}$, the commutators in the Lindblad disturbance approximately vanish, leaving the weak value expression as the conditioned average [24]. Evidently from this analysis, it is clear that any situation in which the Lindblad disturbance can be made irrelevant in the numerator will be able to recover a generalized weak value as an operational average, up to renormalization. It thus becomes interesting to consider special cases where stronger measurements with less statistical uncertainty can recover the weak value expression without any approximations.

Here, we present an interferometric experiment in which the neutron's path degree of freedom is characterized by both weak measurements and stronger generalized measurements that can recover the same weak value expression. Moreover, we provide a detailed analysis of how to obtain not only the real part of a weak value, but also the imaginary part and the modulus directly using experimentally collected intensities at any interaction strength. This result extends the idea of generalized eigenvalues by canceling the measurement perturbation through a strategic renormalization procedure. The observable of interest is the Pauli operator $\hat{\sigma}_z^\mathrm{p}$ associated with the path of the neutron, and the spin has the role of the meter system or measurement device, or *pointer*. The weak values obtained through weak measurements, denoted $\langle \hat{\sigma}_z^\mathrm{p} \rangle_\mathrm{w}$, are then compared to the weak values obtained through stronger generalized measurements, denoted $\langle \hat{\sigma}_z^\mathrm{p} \rangle_\mathrm{g}$. The precision as well as the accuracy of both experimental approaches for obtaining the same quantity are then discussed in detail.

3. Experimental procedure

The measurement scheme starts with the initial state of the composite system, consisting of both the system that shall be measured—path—and the probe or meter system—spin

$$|\Psi_\mathrm{i}\rangle = |\mathrm{P_i}\rangle\,|\mathrm{S_i}\rangle = \frac{1}{\sqrt{2}}\left(|\mathrm{P}_z;+\rangle + |\mathrm{P}_z;-\rangle\right)|\mathrm{S}_x;+\rangle\,, \tag{3}$$

where $|\mathrm{P_i}\rangle$ is the initial path and $|\mathrm{S_i}\rangle$ the initial spin state. $|\mathrm{P}_z;+\rangle$ and $|\mathrm{P}_z;-\rangle$ are the eigenstates of path *I* and *II* respectively, with the corresponding probability amplitude $\frac{1}{\sqrt{2}}$ accounting for a equally weighted coherent superposition of the two beam paths. $|\mathrm{S}_x;+\rangle$ denotes a spin state that is aligned along the positive *x*-axis. A general form for a preselected path state after the first plate of the interferometer (50:50 beam splitter), which is depicted in Fig. 1, is given by

$$|\mathrm{P_i}\rangle = \frac{1}{\sqrt{2}}\left(|\mathrm{P}_z;+\rangle + e^{\mathrm{i}\chi}\,|\mathrm{P}_z;-\rangle\right), \tag{4}$$

where χ represents the relative phase between the path eigenstates.

Eq. (3) describes a completely separable state, since there is no coupling between the spin and path. In the next step a coupling by a unitary evolution accounting for path-dependent spin rotations is induced. Strictly speaking: the spin is rotated by a certain angle α about the *z*-axis in the *xy*-plane with clockwise (positive) rotation in path *I* and counter clockwise (negative) rotation in path *II*. The corresponding interaction Hamiltonian is expressed as

$$\widehat{H}_\mathrm{int} = -\vec{\mu}\cdot\vec{B}\;\widehat{\Pi}_{z+}^\mathrm{p} + \vec{\mu}\cdot\vec{B}\;\widehat{\Pi}_{z-}^\mathrm{p} = -\mu B_z^{\pm\alpha}\,\hat{\sigma}_z^\mathrm{s}\hat{\sigma}_z^\mathrm{p} \tag{5}$$

where $\widehat{\Pi}_{z\pm}^\mathrm{p}$ are the projection operators on the path eigenstates $|\mathrm{P}_z;+\rangle$ and $|\mathrm{P}_z;-\rangle$, $\vec{\mu} = \mu\vec{\sigma}^\mathrm{s}$, where μ is the neutron's magnetic moment and $\vec{B} = \left(0, 0, B_z^{\pm\alpha}\right)$ an applied magnetic field. The Pauli operators for spin and path are given by $\hat{\sigma}_z^\mathrm{s} = |\mathrm{S}_z;+\rangle\langle\mathrm{S}_z;+| - |\mathrm{S}_z;-\rangle\langle\mathrm{S}_z;-|$ and $\hat{\sigma}_z^\mathrm{p} = |\mathrm{P}_z;+\rangle\langle\mathrm{P}_z;+| - |\mathrm{P}_z;-\rangle\langle\mathrm{P}_z;-|$, respectively. The action of $\widehat{H}_\mathrm{int}$ on the composite system $|\Psi_\mathrm{i}\rangle$ is described by its time evolution denoted as

$$|\Psi'\rangle = \mathrm{e}^{\frac{-\mathrm{i}}{\hbar}\int \widehat{H}_\mathrm{int}\mathrm{d}t}\,|\Psi_\mathrm{i}\rangle = \mathrm{e}^{\frac{-\mathrm{i}\alpha\hat{\sigma}_z^\mathrm{s}\hat{\sigma}_z^\mathrm{p}}{2}}\,|\Psi_\mathrm{i}\rangle\,, \tag{6}$$

where α is the angle of rotation given by $\alpha = \frac{-2\mu B_z \tau}{\hbar}$, with τ being the time the neutron's is exposed to the magnetic field region. Note that α is the relevant parameter accounting for the interaction strength of the measurement and $\hat{\sigma}_z^\mathrm{s}$ is the generator of spin rotations about the *z*-axis.

In the standard weak measurement procedure [1], as applied in our previous experiment [30], the evolution operator $\exp\left(\frac{-\mathrm{i}\alpha\hat{\sigma}_z^\mathrm{s}\hat{\sigma}_z^\mathrm{p}}{2}\right)$ is series expanded around α. By neglecting higher orders of α consequently an approximation for $\alpha \ll 1$ was made there. In contrast, here, however the analytical relation $\exp\left(\frac{-\mathrm{i}\alpha\hat{\sigma}_z^\mathrm{s}\hat{\sigma}_z^\mathrm{p}}{2}\right) = \cos\frac{\alpha}{2} - \mathrm{i}\hat{\sigma}_z^\mathrm{s}\hat{\sigma}_z^\mathrm{p}\sin\frac{\alpha}{2}$ is used [13]—hence no approximation is made in present work. Consequently the calculations hold for arbitrary interaction strengths, i.e., arbitrary rotation angles α. The analytic form of the state after the interaction is given by

$$\left|\Psi'\right\rangle = \cos\frac{\alpha}{2}\,|\mathrm{P_i}\rangle\,|\mathrm{S}_x;+\rangle - \mathrm{i}\hat{\sigma}_z^\mathrm{p}\sin\frac{\alpha}{2}\,|\mathrm{P_i}\rangle\,|\mathrm{S}_x;-\rangle \tag{7}$$

The last step of the measurement procedure is the post-selection of the final path state which is

$$|\mathrm{P_f}\rangle = |\mathrm{P}_x;+\rangle = \frac{1}{\sqrt{2}}\left(|\mathrm{P}_z;+\rangle + |\mathrm{P}_z;-\rangle\right), \tag{8}$$

where the action of the path post-selection is equivalent to a projection onto $|\mathrm{P_f}\rangle\langle\mathrm{P_f}|$. This yields the final state of the composite system $|\Psi_\mathrm{f}\rangle$, given by

$$|\Psi_\mathrm{f}\rangle = \langle\mathrm{P_f}|\mathrm{P_i}\rangle\left[\cos\frac{\alpha}{2}\,|\mathrm{S}_x;+\rangle - \mathrm{i}\,\sin\frac{\alpha}{2}\left\langle\hat{\sigma}_z^\mathrm{p}\right\rangle_\mathrm{w}|\mathrm{S}_x;-\rangle\right]|\mathrm{P_f}\rangle, \tag{9}$$

with $\langle\hat{\sigma}_z^\mathrm{p}\rangle_\mathrm{w} \equiv \frac{\langle\mathrm{P_f}|\hat{\sigma}_z^\mathrm{p}|\mathrm{P_i}\rangle}{\langle\mathrm{P_f}|\mathrm{P_i}\rangle}$. Finally, the weak value of the neutron path operator $\hat{\sigma}_z^\mathrm{p}$ is determined by evaluating the pointer system, that is represented by the neutron's spin. Projective measurements along the six spin directions $\pm x$, $\pm y$ and $\pm z$, yield six intensities $I_{j\pm} = \left|\langle\mathrm{S}_j;\pm|\Psi_\mathrm{f}\rangle\right|^2$ with

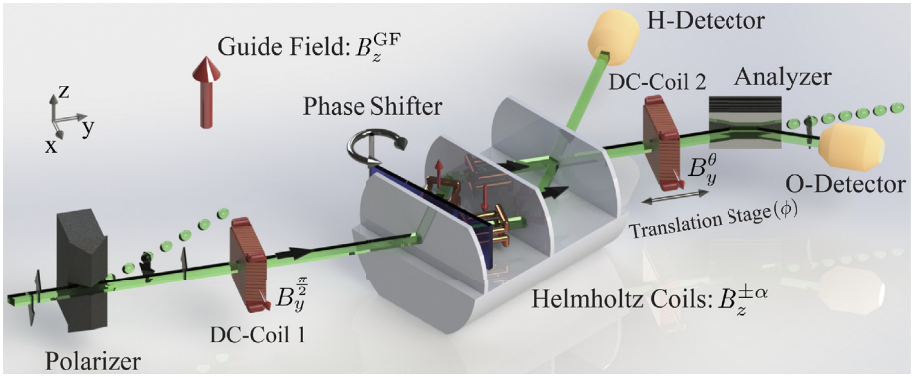

Fig. 1. Neutron interferometric setup for determination of real and imaginary, as well as modulus, of the path's weak value measured both weakly $\langle\hat{\sigma}_z^{\rm p}\rangle_{\rm w}$ and with stronger generalized measurements $\langle\hat{\sigma}_z^{\rm p}\rangle_{\rm g}$. The incident beam is already monochromatic with wavelength $\lambda_0 = 1.91$ Å, due to reflection from a perfect silicon monochromator (not depicted in this figure). The individual neutron optical components are explained in the main text, as well as in Figs. 3 and 4.

($j = x, y, z$), which allow for extraction of the imaginary and real part as well as the modulus of the path operator's weak value $\langle\hat{\sigma}_z^{\rm p}\rangle_{\rm w}$. They are given explicitly by

$$I_{x+} = |\langle {\rm S}_x; +|\Psi_{\rm f}\rangle|^2 = |\langle {\rm P_f}|{\rm P_i}\rangle|^2 \cos^2\frac{\alpha}{2} \tag{10a}$$

$$I_{x-} = |\langle {\rm S}_x; -|\Psi_{\rm f}\rangle|^2 = |\langle {\rm P_f}|{\rm P_i}\rangle|^2 \sin^2\frac{\alpha}{2}\,|\langle\hat{\sigma}_z^{\rm p}\rangle_{\rm w}|^2 \tag{10b}$$

$$I_{y+} = |\langle {\rm S}_y; +|\Psi_{\rm f}\rangle|^2 = \frac{|\langle {\rm P_f}|{\rm P_i}\rangle|^2}{4}\left(1 + \cos\alpha + (1-\cos\alpha)|\langle\hat{\sigma}_z^{\rm p}\rangle_{\rm w}|^2 + 2\,{\rm Re}\left\langle\hat{\sigma}_z^{\rm p}\right\rangle_{\rm w}\sin\alpha\right) \tag{10c}$$

$$I_{y-} = |\langle {\rm S}_y; -|\Psi_{\rm f}\rangle|^2 = \frac{|\langle {\rm P_f}|{\rm P_i}\rangle|^2}{4}\left(1 + \cos\alpha + (1-\cos\alpha)|\langle\hat{\sigma}_z^{\rm p}\rangle_{\rm w}|^2 - 2\,{\rm Re}\left\langle\hat{\sigma}_z^{\rm p}\right\rangle_{\rm w}\sin\alpha\right) \tag{10d}$$

$$I_{z+} = |\langle {\rm S}_z; +|\Psi_{\rm f}\rangle|^2 = \frac{|\langle {\rm P_f}|{\rm P_i}\rangle|^2}{4}\left(1 + \cos\alpha + (1-\cos\alpha)|\langle\hat{\sigma}_z^{\rm p}\rangle_{\rm w}|^2 + 2\,{\rm Im}\left\langle\hat{\sigma}_z^{\rm p}\right\rangle_{\rm w}\sin\alpha\right) \tag{10e}$$

$$I_{z-} = |\langle {\rm S}_z; -|\Psi_{\rm f}\rangle|^2 = \frac{|\langle {\rm P_f}|{\rm P_i}\rangle|^2}{4}\left(1 + \cos\alpha + (1-\cos\alpha)|\langle\hat{\sigma}_z^{\rm p}\rangle_{\rm w}|^2 - 2\,{\rm Im}\left\langle\hat{\sigma}_z^{\rm p}\right\rangle_{\rm w}\sin\alpha\right). \tag{10f}$$

Combining the individual equations from above yields the respective relations for real and imaginary part of the weak value of $\hat{\sigma}_z^{\rm p}$, as well as its modulus as

$${\rm Re}\left\langle\hat{\sigma}_z^{\rm p}\right\rangle_{\rm w} = \frac{1}{2}\cot\left(\frac{\alpha}{2}\right)\frac{I_{y+} - I_{y-}}{I_{x+}} \tag{11a}$$

$${\rm Im}\left\langle\hat{\sigma}_z^{\rm p}\right\rangle_{\rm w} = \frac{1}{2}\cot\left(\frac{\alpha}{2}\right)\frac{I_{z+} - I_{z-}}{I_{x+}} \tag{11b}$$

$$\left|\left\langle\hat{\sigma}_z^{\rm p}\right\rangle_{\rm w}\right| = \cot\left(\frac{\alpha}{2}\right)\sqrt{\frac{I_{x-}}{I_{x+}}}. \tag{11c}$$

At this point we want to emphasize that no approximations are made to derive these expressions. As a consequence, the relations (11a) to (11c) hold for any value of the spin rotation angle α, i.e., for arbitrary measurement strengths. In the case of stronger generalized measurements with $\alpha \not\ll 1$ we will denote the obtained quantity as $\langle\hat{\sigma}_z^{\rm p}\rangle_{\rm g}$ to contrast it with the standard weakly measured value $\langle\hat{\sigma}_z^{\rm p}\rangle_{\rm w}$ with $\alpha \ll 1$.

To connect these expressions with the previous generalized eigenvalue results discussed in the introduction, we focus on the real part of the weak value in Eq. (11a). Noting that this real part is obtained from the relative y intensities, we re-examine the structure of the y-intensity expressions. Recall that the initial spin state is $|{\rm S}_x; +\rangle$, and the path-spin interaction can be written $\hat{U}_\alpha = \cos\frac{\alpha}{2} - {\rm i}\hat{\sigma}_z^{\rm s}\hat{\sigma}_z^{\rm p}\sin\frac{\alpha}{2}$. As such, if the y spin basis is measured, the path degree of freedom will be affected by the Kraus operators

$$\hat{M}_{y\pm} = \langle {\rm S}_y; \pm|\hat{U}_\alpha|{\rm S}_x; +\rangle = \frac{e^{\mp {\rm i}\pi/4}}{\sqrt{2}}\left[\cos\frac{\alpha}{2} \pm \hat{\sigma}_z^{\rm p}\sin\frac{\alpha}{2}\right] \tag{12}$$

such that the associated POVM elements are

$$\hat{E}_{y\pm} = \hat{M}_{y\pm}^\dagger\hat{M}_{y\pm} = \frac{1}{2}\left[1 \pm \hat{\sigma}_z^{\rm p}\sin\alpha\right]. \tag{13}$$

It is then clear that assigning the values $\beta_{y\pm} = \pm 1/\sin\alpha$ produces the operator identity

$$\sum_{y\pm}\beta_{y\pm}\hat{E}_{y\pm} = \hat{\sigma}_z^{\rm p} \tag{14}$$

indicating that $\beta_{y\pm}$ are the appropriate generalized eigenvalues to assign the spin pointer in the basis of y in order to measure $\hat{\sigma}_z^{\rm p}$.

The conditioned average of generalized eigenvalues given the initial and final path states is

$$\sum_{y\pm}\beta_{y\pm}p(y \pm |{\rm i}, {\rm f}) = \frac{1}{\sin\alpha}\frac{I_{y+} - I_{y-}}{I_{y+} + I_{y-}} \tag{15}$$

using the intensities

$$I_{y\pm} = |\langle {\rm P_f}|\,\hat{M}_{y\pm}\,|{\rm P_i}\rangle|^2 = \frac{|\langle {\rm P_f}|{\rm P_i}\rangle|^2}{4}\left(1 + \cos\alpha + (1-\cos\alpha)|\langle\hat{\sigma}_z^{\rm p}\rangle_{\rm w}|^2 \pm 2\,{\rm Re}\left\langle\hat{\sigma}_z^{\rm p}\right\rangle_{\rm w}\sin\alpha\right), \tag{16}$$

equivalent to Eqs. (10c) and (10d). The conditioned average then yields

$$\frac{1}{\sin\alpha}\frac{I_{y+} - I_{y-}}{I_{y+} + I_{y-}} = \frac{2\,{\rm Re}\langle\hat{\sigma}_z^{\rm p}\rangle_w}{1 + |\langle\hat{\sigma}_z^{\rm p}\rangle_w|^2 - (|\langle\hat{\sigma}_z^{\rm p}\rangle_w|^2 - 1)\cos\alpha}, \tag{17}$$

which converges to the real part of the weak value in the limit $\alpha \to 0$, consistent with the general conclusions of Refs. [22–24].

The key insight that extends this idea to the exact intensity expression in Eq. (11a) is that the denominator of Eq. (17) can be exactly canceled by renormalizing the intensity difference not by the y-intensity sum, but rather with an appropriately weighted I_{x+}. This corrected renormalization then recovers the exact weak value expression for any interaction strength α. Moreover, similar renormalization insights recover the other two exact expressions in Eqs. (11b) and (11c).

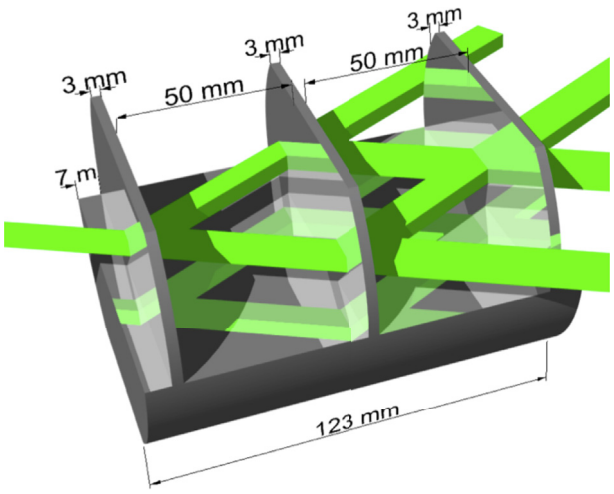

Fig. 2. Dimensions of the applied triple Laue (LLL) neutron interferometer. The interferometer is cut from a single ingot of a silicon perfect crystal. Three blades are machined and left attached to a common silicon base to maintain the perfect alignment of all Si atoms in the single crystal.

4. Experimental realization

The experiment was carried out at the neutron interferometer instrument S18 at the high-flux reactor of the Institute Laue-Langevin (ILL) in Grenoble, France. A schematic illustration of the interferometric setup is depicted in Fig. 1. The dimensions of the applied triple Laue (LLL) neutron interferometer are given in Fig. 2. A monochromatic beam with mean wavelength $\lambda_0 = 1.91$ Å ($\lambda/\lambda_0 \sim 0.02$) and 5×5 mm^2 beam cross section, is selected by a triple bounce silicon perfect crystal monochromator (not shown in Fig. 1) from am white beam. The beam is polarized by a birefringent magnetic field prism in + z-direction (≅1 T), since, owing to the angular separation at the deflection (a few seconds of arc for the parallel and anti-parallel spin state), the interferometer is adjusted so that only the spin-up component fulfills the Bragg condition at the first interferometer plate.

4.1. Pre-selection

After passing the magnetic field prism, the neutrons enter a static magnetic guide field set to 13G, covering the entire setup, which points in the +z-direction and prevents depolarization. Before the neutron beam enters the interferometer, the neutron's spin is rotated into the x-direction by DC Coil 1 carrying out a $\frac{\pi}{2}$ spin-rotation, which is illustrated in Fig. 3. The spin turner consists of a DC coil which produces a static magnetic field B_y pointing in y-direction and a perpendicular (outer) coil in z-direction, which is adjusted such that it exactly compensates the contribution of the magnetic guide field. Within the DC coil, the spin precesses about the y-axis due to Larmor precession about the magnetic field axes. $B_y^{\pi/2}$ is adjusted such that it induces a $\frac{\pi}{2}$ spin-rotation, thereby preparing the initial spin state of the probe system $|\mathrm{S_i}\rangle = |\mathrm{S_x};+\rangle$. To tune the relative phase χ between the orthogonal path eigenstates, a parallel sided sapphire slab is inserted between the first and the second plate of the interferometer as a phase shifter. By rotating the phase shifter plate $\chi = -N_{\mathrm{ps}} b_c \lambda D$ (with the thickness of the phase shifter plate D, the neutron wavelength λ, the coherent scattering length b_c and the particle density N_{ps} in the phase shifter plate) can be tuned systematically due to the different relative path lengths in path I and II. So the purpose of the phase shifter is to tune the initial path state as described in Eq. (4) thereby completing the pre-selection yielding the pre-selected path state $|\mathrm{P_i}\rangle = \frac{1}{\sqrt{2}}\left(|\mathrm{P_z};+\rangle + e^{i\chi}|\mathrm{P_z};-\rangle\right)$

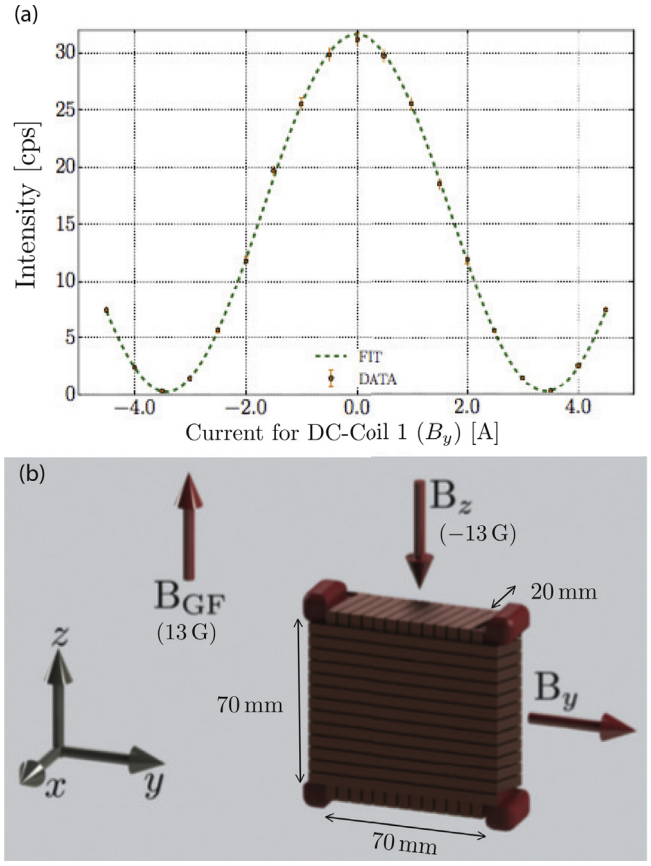

Fig. 3. (a) B_y field scan of DC-Coil 1 with a suitable compensation field $B_z = -13$G. The current of the local minimum (π-flip) corresponds to a field of $B_y = 17.6$G. For a $\pm\frac{\pi}{2}$-rotation half of this field (±8.8G) is required. (b) Design of the spin rotator coil: two layers of wires are wound perpendicular to each other, so that magnetic fields in the z and y-directions can be created.

4.2. Tunable interaction strength

Inside the interferometer, right before the middle plate, a coil in Helmholtz configuration in each beam path enables us to perform path-dependent spin rotations, coupling the neutron's path and spin [29]. The coils, placed inside temperature-controlled and water filled boxes, produce additional magnetic fields in the ± z-direction causing the neutron spins' Larmor precession frequency ω_{L} to decrease or increase depending on the sign of the field, which is minus for path I and plus for path II. The strength of the magnetic field determines the magnitude of the rotation angle α, accounting for the interaction-strength, which is illustrated in Fig. 4. The experiment is performed with two different values of α: to test the interaction in a weak regime α is set to $15 \pm 1°$, which corresponds to a magnetic field $B_z^{\pm\alpha=15(1)^\circ} = 1.9$ G. For the strong interaction α is set to $90 \pm 2°$, which corresponds to the maximum measurement strength (due to the orthogonality of the spin states after the interaction) with $B_z^{\pm\alpha=90(2)^\circ} = 11.8$ G. The accuracy of the spin rotation angles is obtained from the fit parameters from Fig. 4(a).

4.3. Post-selection and pointer read-out

At the interferometer's third plate the beams are recombined by which the path post-selection is carried out. Only neutrons leaving the interferometer in the forward direction with a relative phase $\chi = 0$, denoted as $|\mathrm{P_f}\rangle = \frac{1}{\sqrt{2}}(|\mathrm{P_z};+\rangle + |\mathrm{P_z};-\rangle)$ are spin analyzed. This procedure is called pointer read-out of the probe system (in our case the spin). The spin analysis is performed by a second DC coil mounted on

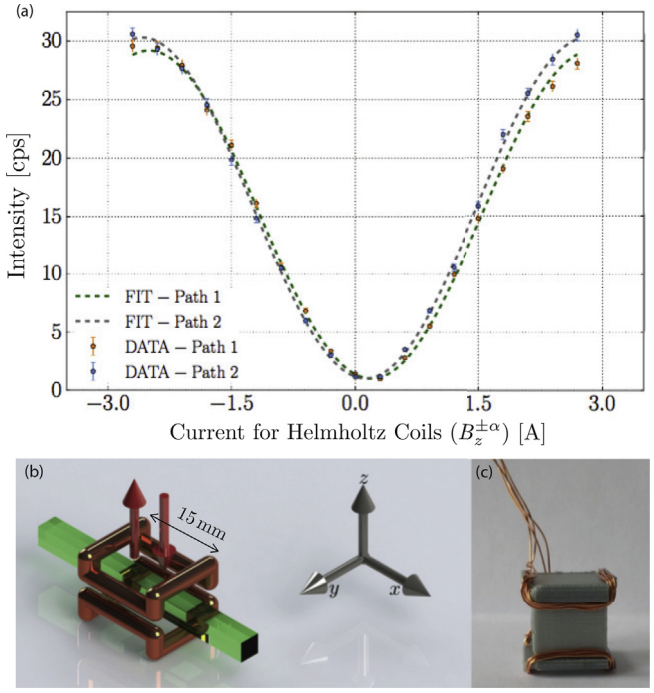

Fig. 4. (a) Current scan of the spin manipulators inside the interferometer: If a current is applied to the Helmholtz coils inside the interferometer they cause an additional Larmor precession of the neutron's spin in the *xy*-plane leading to a change of the azimuth angle ϕ. A rotation of $\phi = \pi$ corresponds to a magnetic field of $B_z^{\pm\alpha=\pi} = 23.6$ G. (b) Depiction of an altered Helmholtz coil pair with the beam (green) at the center. (c) Photograph of an actual coil pair on a 3D printed frame, which is inserted into a water-filled, temperature controlled box. (For interpretation of the references to colour in this figure legend, the reader is referred to the Web version of this article.)

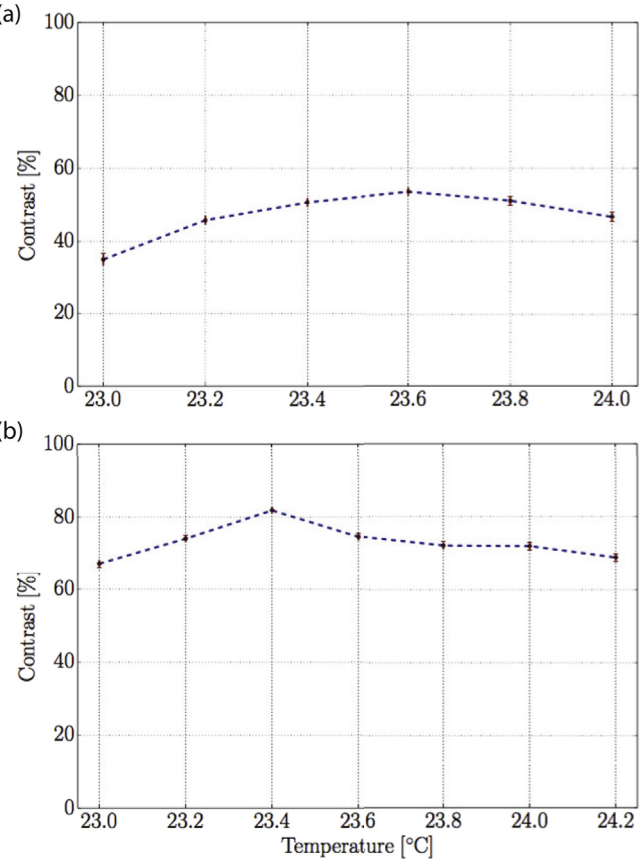

Fig. 5. (a) Observed contrast as a function of the guide field temperature and (b) contrast as a function of the temperature of the spin manipulators inside the interferometer. The temperature of the cooling water is changed each time before a phase shifter scan is performed. Error bars indicate ± one standard deviation of the measured interferometer contrast.

a translation stage in combination with a CoTi supermirror. Inside the coil a tunable magnetic field rotates the spin by a polar angle θ. Hence, for spin analysis direction $\pm z$ the polar angle θ is set to 0 and π, respectively. Depending on the coil's position along the neutrons' trajectory, the spin's azimuth angle ϕ is tuned due to the spin's Larmor precession within the magnetic guide field. Thus for spin analysis direction $\pm x$ a polar angle $\theta = \pm\frac{\pi}{2}$ and azimuthal $\phi = \frac{\pi}{2}$ is chosen. Finally for $\pm y$ we have $\theta = \pm\frac{\pi}{2}$ and $\phi = 0$. Subsequently the supermirror array (together with DC-coil 2) carries out a projective measurement along the direction defined by θ and ϕ of our probe system that is the neutron's spin. In a final step the neutrons are detected by a ^{3}He counter (O-detector). Starting from a beam cross section of 5×5 mm^2 and taking the beam broadening at each of the three interferometer plates into account (depicted Fig. 2), a final (maximal) flux of ~ 50 neutrons cm^{-2} s^{-1} is recorded at the O-detector.

The neutron interferometer is extremely sensitive to thermal fluctuations. All heat generating devices, such as the magnetic guide field or the spin manipulator inside the interferometer, are cooled with temperature controlled water. Fig. 5 illustrates the sensitivity of the neutron interferometer's contrast on these temperature parameters. In Fig. 5(a) the temperature of the guide field's cooling water is varied and subsequently phase shifter scans are performed from which the contrast is determined. The highest value in contrast indicates the correct optimum temperature. In Fig. 5(b) the same procedure is applied to the cooling water of the spin manipulators inside the interferometer.

The intensity modulations $I_{j\pm}$, with $j = x, y, z$, of both measurement strengths, i.e., for weak and strong interaction, are depicted in Fig. 6. Note that the index j denotes the measurement direction of our probe system—the neutron's spin, while a change in χ alters the initial state $|\mathrm{P_i}\rangle = \frac{1}{\sqrt{2}}\left(|\mathrm{P}_z;+\rangle + e^{i\chi}|\mathrm{P}_z;-\rangle\right)$ of the path. Given the initial state of the composite system (path and probe system spin) $|\Psi_\mathrm{i}\rangle = |\mathrm{P_i}\rangle|\mathrm{S_i}\rangle$ from Eq. (3), the evolution operator $\widehat{H}_\mathrm{int}$ of Eq. (5) and the post-selected path state $|\mathrm{P_f}\rangle$ of Eq. (8) it is possible to analytically calculate $I_{j\pm}$, with $j = x, y, z$ for ideal circumstances. The intensities are given by

$$I_{x+} = \cos^2\frac{\alpha}{2}\cos^2\frac{\chi}{2} \tag{18a}$$

$$I_{x-} = \sin^2\frac{\alpha}{2}\sin^2\frac{\chi}{2} \tag{18b}$$

$$I_{y+} = I_{y-} = \frac{1}{4}(1 + \cos\alpha\cos\chi) \tag{18c}$$

$$I_{z+} = \frac{1}{4}(1 + \cos(\alpha + \chi)) \tag{18d}$$

$$I_{z-} = \frac{1}{4}(1 + \cos(\alpha - \chi)). \tag{18e}$$

The six panels in Fig. 6(a) show the interferograms of the weak interaction ($\alpha = 15°$). For I^w_{x+} both the pre- and post-selected spin state are $|\mathrm{S}_x;+\rangle$, yielding a large count rate, whereas the count rate of I^w_{x-} is very low, since initial and final spin states are orthogonal. $I^\mathrm{w}_{y\pm}$ are identical having half of the maximal count rate. Finally $I^\mathrm{w}_{z\pm}$ are phase shifted by two times α also at half of the maximal count rate. In the six panels of Fig. 6(b) the interferograms for the strong interaction are shown. Resulting from the large spin rotation of $\alpha = \pm 90°$ in each beam path, $I^\mathrm{st}_{x\pm}$ now show the same average count rate, but are phase shifted by π. $I^\mathrm{st}_{y\pm}$ now show almost no contrast at all for strong interaction strength. The phase shift between I^st_{z+} and I^st_{z-} is now also π and therefore easy to resolve.

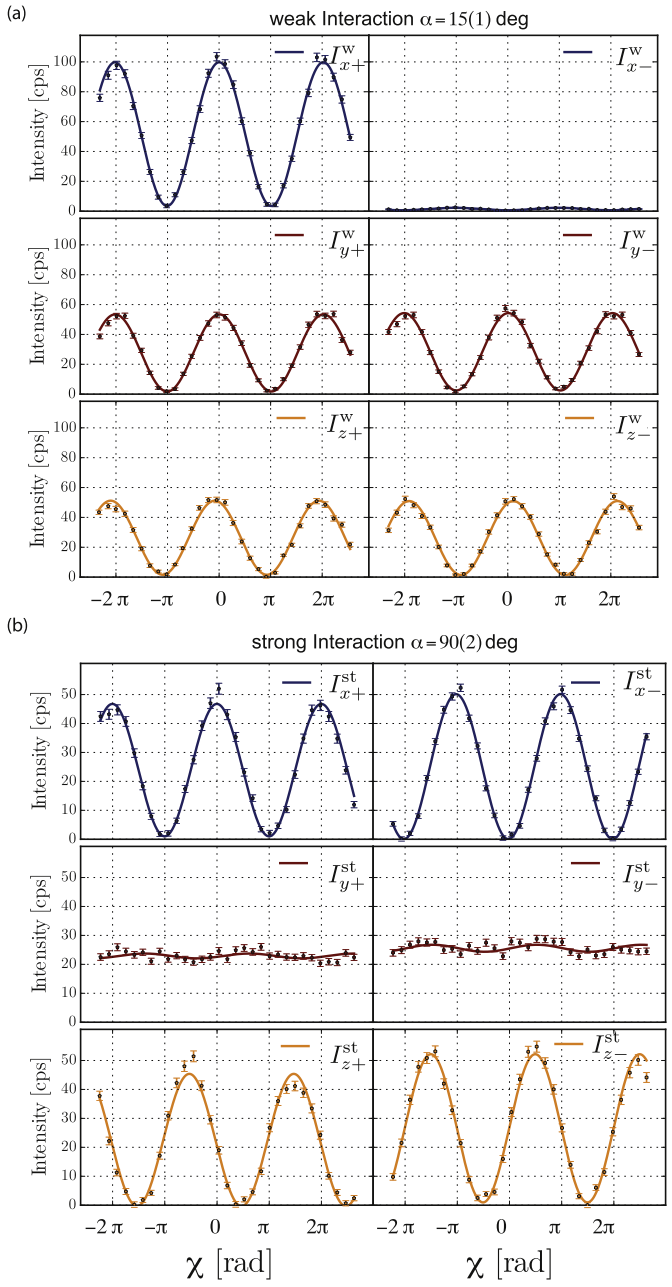

Fig. 6. Intensity modulations due to rotation of the phase shifter observed for pin analysis directions $\pm x$, $\pm y$ and $\pm z$. In (a) interferograms for weak interaction ($\alpha = 15 \pm 1)°$) are plotted and in (b) for strong interaction ($\alpha = 90 \pm 2°$).

5. Results

For the extraction of the imaginary part of $\langle\hat{\sigma}_z^{\mathrm{p}}\rangle_{\mathrm{w}}$ [and $\langle\hat{\sigma}_z^{\mathrm{p}}\rangle_{\mathrm{g}}$] the intensities $I_{z\pm}$ and I_{x+} are required. Here I_{x+} acts as a normalization factor, while resolving the phase shift between I_{z+} and I_{z-} is crucial for determination of $\Im\langle\hat{\sigma}_z^{\mathrm{p}}\rangle_{\mathrm{w}}$ [and $\Im\langle\hat{\sigma}_z^{\mathrm{p}}\rangle_{\mathrm{g}}$]. Since this phase shift is expected to be two times α, it is much harder to resolve in the weak interaction case, which is depicted in Fig. 7(a) middle panel, compared to the stronger generalized measurements $\Im\langle\hat{\sigma}_z^{\mathrm{p}}\rangle_{\mathrm{g}}$ with maximal interaction strength ($\alpha = 90°$) from Fig. 7(b).

Similarly $\Re\langle\hat{\sigma}_z^{\mathrm{p}}\rangle_{\mathrm{w}}$, as well as $\Re\langle\hat{\sigma}_z^{\mathrm{p}}\rangle_{\mathrm{g}}$, (Fig. 7(a,b) top panels) are extracted from the intensities $I_{y\pm}$ and I_{x+}. Since theory predicts the value to be zero, I_{y+} and I_{y-} are very close or even equal. Furthermore the interferograms of $I_{y\pm}$ lose contrast for increasing α, due to the spin rotation inside the interferometer approach towards an orthogonal spin

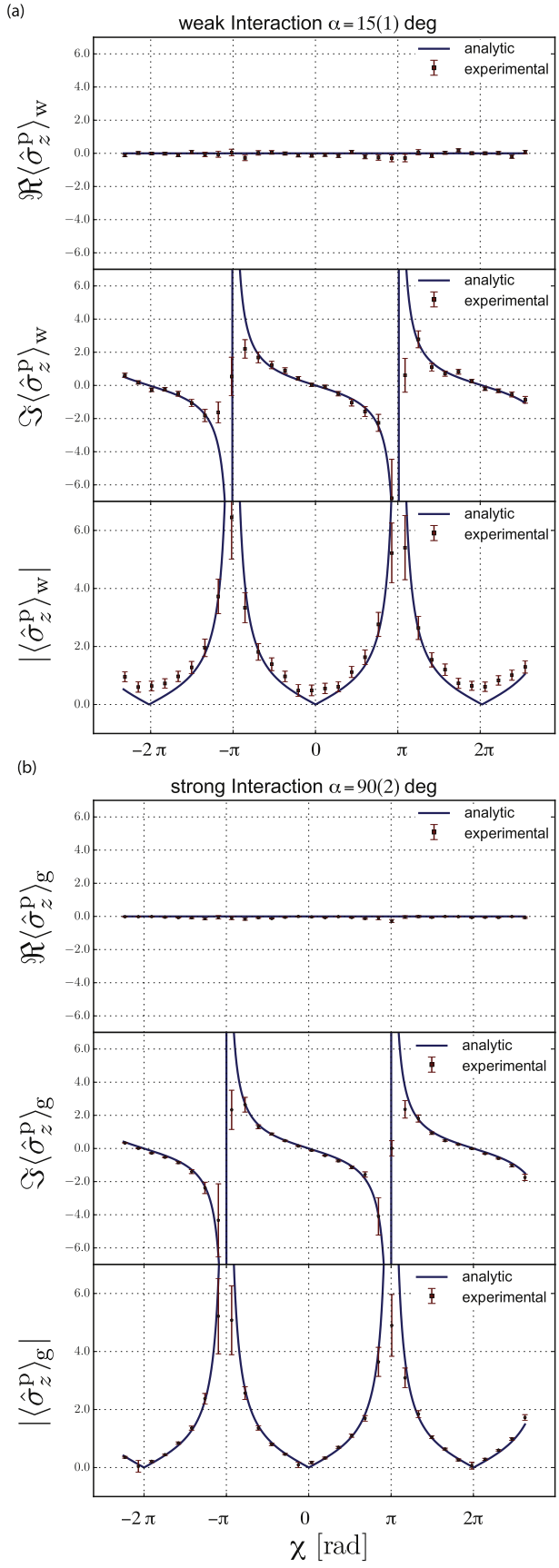

Fig. 7. Real, Imaginary and modulus of the path observable $\hat{\sigma}_z$. In (a) weak measurements ($\alpha = 15°$) yield the weak value $\langle\hat{\sigma}_z\rangle_{\mathrm{w}}$, whereas in (b) stronger generalized measurements ($\alpha = 90°$) are used to produce $\langle\hat{\sigma}_z\rangle_{\mathrm{g}}$.

state. For $\alpha = 90°$ the spin state is completely orthogonal and thus no contrast is observed (see Fig. 6(b) middle panel).

Finally the modulus of $\langle\hat{\sigma}_z^{\mathrm{p}}\rangle_{\mathrm{w}}$ and $\langle\hat{\sigma}_z^{\mathrm{p}}\rangle_{\mathrm{g}}$ (Fig. 7(a,b) bottom panels) are directly obtained from the $I_{x\pm}$ data: they are proportional to the square root of I_{x-}/I_{x+}. The advantage of the strong interaction is intuitively understood: the discrimination of the relevant signal from the background is crucial, for $\alpha = 0°$ I_{x-} is expected to be zero and the signal becomes larger with increasing α.

While both measurements are in good agreement with the theoretical predictions, the strong measurement results are significantly better, in terms of precision, which is a measure of fluctuation (size of errorbars), and accuracy, being a measure of deviation from the theoretical prediction. The strong interaction scheme outperforms the weak one in both accuracy and precision for all settings of experimentally determined parameters. Especially for the modulus the superiority of $\langle\hat{\sigma}_z^{\mathrm{p}}\rangle_{\mathrm{g}}$ over the weakly measured $\langle\hat{\sigma}_z^{\mathrm{p}}\rangle_{\mathrm{w}}$ becomes apparent when comparing the resulting plots. There is another important experimental factor that has to be taken into account and that is the measurement time. To resolve the small phase shifts between I_{z+} and I_{z-} as well as to distinguish I_{x-} from the background long counting times were necessary for the weak interaction. For each point on the weak interaction ($\alpha = 15°$) curve a counting time of 540 s was necessary, while 290 s were sufficient for the strong one ($\alpha = 90°$).

Our protocol for determination of weak values makes it possible to obtain weak values of a two-level quantum system with high accuracy and arbitrary interaction (measurement) strength. Increasing the measurement strength provides a clear discrimination of small signals from background which is of particular significance whenever dealing with low count rates.

6. Conclusions and outlook

In summary, we have presented a weak value determination scheme via arbitrary interaction strengths and applied it to experimentally determine weak values, using generalized measurements with both weak interactions and strong interactions. Experimental evidence is given that strong interactions are superior to weak interactions in terms of accuracy and precision, as well as required measurement time. Our measurement scheme is not limited to the neutron's spin and path, but is in fact completely general and can be used for any coupling between two two-level quantum systems.

Acknowledgments

We acknowledge support by the Austrian Science Fund (FWF) Project Nos. P30677-N20 & P25795-N20. Furthermore we thank the ILL in Grenoble for its hospitality and continuous support.

References

[1] Y. Aharonov, D.Z. Albert, L. Vaidman, How the result of a measurement of a component of the spin of a spin-1/2 particle can turn out to be 100, Phys. Rev. Lett. 60 (1988) 1351–1354, http://link.aps.org/doi/10.1103/PhysRevLett.60.1351.

[2] J. Dressel, M. Malik, F.M. Miatto, A.N. Jordan, R.W. Boyd, *Colloquium* : understanding quantum weak values: basics and applications, Rev. Mod. Phys. 86 (2014) 307–316, http://link.aps.org/doi/10.1103/RevModPhys.86.307.

[3] O. Hosten, P. Kwiat, Observation of the spin hall effect of light via weak measurements, Science 319 (2008) 787–790, http://www.sciencemag.org/content/319/5864/787.abstract.

[4] P.B. Dixon, D.J. Starling, A.N. Jordan, J.C. Howell, Ultrasensitive beam deflection measurement via interferometric weak value amplification, Phys. Rev. Lett. 102 (2009) 173601, http://link.aps.org/doi/10.1103/PhysRevLett.102.173601.

[5] D.J. Starling, P.B. Dixon, A.N. Jordan, J.C. Howell, Precision frequency measurements with interferometric weak values, Phys. Rev. A 82 (2010) 063822, http://link.aps.org/doi/10.1103/PhysRevA.82.063822.

[6] D.J. Starling, P.B. Dixon, N.S. Williams, A.N. Jordan, J.C. Howell, Continuous phase amplification with a Sagnac interferometer, Phys. Rev. A 82 (2010) 011802, http://link.aps.org/doi/10.1103/PhysRevA.82.011802.

[7] A. Feizpour, X. Xing, A.M. Steinberg, Amplifying single-photon nonlinearity using weak measurements, Phys. Rev. Lett. 107 (2011) 133603, http://link.aps.org/doi/10.1103/PhysRevLett.107.133603.

[8] L. Zhou, Y. Turek, C.P. Sun, F. Nori, Weak-value amplification of light deflection by a dark atomic ensemble, Phys. Rev. A 88 (2013) 053815, http://link.aps.org/doi/10.1103/PhysRevA.88.053815.

[9] S. Kocsis, B. Braverman, S. Ravets, M.J. Stevens, R.P. Mirin, L.K. Shalm, A.M. Steinberg, Observing the average trajectories of single photons in a two-slit interferometer, Science 332 (2011) 1170–1173, http://www.sciencemag.org/content/332/6034/1170.abstract.

[10] J.S. Lundeen, B. Sutherland, A. Patel, C. Stewart, C. Bamber, Direct measurement of the quantum wavefunction, Nature (London) 474 (2011) 188–191, http://www.nature.com/nature/journal/v474/n7350/full/nature10120.html?foxtrotcallback=true.

[11] M.E. Goggin, M.P. Almeida, M. Barbieri, B.P. Lanyon, J.L. O'Brien, A.G. White, G.J. Pryde, Violation of the Leggett-Garg inequality with weak measurements of photons, Proc. Natl. Acad. Sci. U.S.A. 108 (2011) 1256–1261, http://www.pnas.org/content/108/4/1256.abstract.

[12] L.A. Rozema, A. Darabi, D.H. Mahler, A. Hayat, Y. Soudagar, A.M. Steinberg, Violation of Heisenberg's measurement-disturbance relationship by weak measurements, Phys. Rev. Lett. 109 (2012) 100404, http://link.aps.org/doi/10.1103/PhysRevLett.109.100404.

[13] G. Vallone, D. Dequal, Strong measurements give a better direct measurement of the quantum wave function, Phys. Rev. Lett. 116 (2016) 040502, https://link.aps.org/doi/10.1103/PhysRevLett.116.040502.

[14] T. Denkmayr, H. Geppert, H. Lemmel, M. Waegell, J. Dressel, Y. Hasegawa, S. Sponar, Experimental demonstration of direct path state characterization by strongly measuring weak values in a matter-wave interferometer, Phys. Rev. Lett. 118 (2017) 010402, http://link.aps.org/doi/10.1103/PhysRevLett.118.010402.

[15] J. Resch, J. Lundeen, A.M. Steinberg, Experimental realization of the quantum box problem, Phys. Lett. 324 (2004) 125, http://www.sciencedirect.com/science/article/pii/S0375960104002506?via%3Dihub.

[16] J.S. Lundeen, A.M. Steinberg, Experimental joint weak measurement on a photon pair as a probe of Hardy's paradox, Phys. Rev. Lett. 102 (2009) 020404, http://link.aps.org/doi/10.1103/PhysRevLett.102.020404.

[17] K. Yokota, T. Yamamoto, M. Koashi, N. Imoto, Direct observation of Hardy's paradox by joint weak measurement with an entangled photon pair, N. J. Phys. 11 (2009) 033011, http://stacks.iop.org/1367-2630/11/i=3/a=033011.

[18] Y. Aharonov, A. Botero, S. Popescu, B. Reznik, J. Tollaksen, Revisiting Hardy's paradox: counterfactual statements, real measurements, entanglement and weak values, Phys. Lett. 301 (2002) 130–138, http://www.sciencedirect.com/science/article/pii/S0375960102009866.

[19] Y. Aharonov, S. Popescu, D. Rohrlich, P. Skrzypczyk, Quantum Cheshire cats, N. J. Phys. 15 (2013) 113015, http://stacks.iop.org/1367-2630/15/i=11/a=113015.

[20] T. Denkmayr, H. Geppert, S. Sponar, H. Lemmel, A. Matzkin, J. Tollaksen, Y. Hasegawa, Experimental observation of a quantum Cheshire Cat in matter-wave interferometry, Nat. Commun. 5 (2014) 4492, https://www.nature.com/articles/ncomms5492.

[21] S. Sponar, T. Denkmayr, H. Geppert, Y. Hasegawa, Fundamental features of quantum dynamics studied in matter-wave interferometry—Spin weak values and the quantum Cheshire-Cat, Atoms 4 (2016) 11, http://www.mdpi.com/2218-2004/4/1/11.

[22] J. Dressel, S. Agarwal, A.N. Jordan, Contextual values of observables in quantum measurements, Phys. Rev. Lett. 104 (2010) 240401, https://link.aps.org/doi/10.1103/PhysRevLett.104.240401.

[23] J. Dressel, A.N. Jordan, Contextual-value approach to the generalized measurement of observables, Phys. Rev. A 85 (2011) 022123, https://doi.org/10.1103/PhysRevA.85.022123.

[24] J. Dressel, A.N. Jordan, Quantum instruments as a foundation for both states and observables, Phys. Rev. A 88 (2013) 022107, https://doi.org/10.1103/PhysRevA.88.022107.

[25] J. Dressel, A.N. Jordan, Weak values are universal in Von Neumann measurements, Phys. Rev. Lett. 109 (2012) 230402, https://doi.org/10.1103/PhysRevLett.109.230402.

[26] S. Kochen, E.P. Specker, The problems of hidden variables in quantum mechanics, J. Math. Mech. 17 (1967) 59.

[27] N.D. Mermin, Hidden variables and the two theorems of John Bell, Rev. Mod. Phys. 65 (1993) 803, https://doi.org/10.1103/RevModPhys.65.803.

[28] N.W.M. Ritchie, J.G. Story, R.G. Hulet, Realization of a measurement of a "weak value", Phys. Rev. Lett. 66 (1991) 1107–1110, http://link.aps.org/doi/10.1103/PhysRevLett.66.1107.

[29] H. Geppert, T. Denkmayr, S. Sponar, H. Lemmel, Y. Hasegawa, Improvement of the polarized neutron interferometer setup demonstrating violation of a Bell-like inequality, Nucl. Instrum. Meth. Phys. Res. A 763 (2014) 417–423, http://www.sciencedirect.com/science/article/pii/S0168900214008341.

[30] S. Sponar, T. Denkmayr, H. Geppert, H. Lemmel, A. Matzkin, J. Tollaksen, Weak values obtained in matter-wave interferometry, Phys. Rev. A 92 (2015) 062121, http://link.aps.org/doi/10.1103/PhysRevA.92.062121.

[31] H. Rauch, S.A. Werner, Neutron Interferometry, Clarendon Press, Oxford, 2000.
[32] Y. Hasegawa, R. Loidl, G. Badurek, M. Baron, H. Rauch, Violation of a Bell-like inequality in single-neutron interferometry, Nature (London) 425 (2003) 45–48, http://www.nature.com/nature/journal/v425/n6953/abs/nature01881.html.
[33] D.A. Pushin, M.G. Huber, M. Arif, D.G. Cory, Experimental realization of decoherence-free subspace in neutron interferometry, Phys. Rev. Lett. 107 (2011) 150401, http://link.aps.org/doi/10.1103/PhysRevLett.107.150401.
[34] Y. Hasegawa, H. Rauch, Quantum phenomena explored with neutrons, N. J. Phys. 13 (2011) 115010, http://stacks.iop.org/1367-2630/13/i=11/a=115010.
[35] J. Klepp, S. Sponar, Y. Hasegawa, Fundamental phenomena of quantum mechanics explored with neutron interferometers, Prog. Theor. Exp. Phys. 8 (2014), http://ptep.oxfordjournals.org/content/2014/8/082A01.abstract.